nature photonics

Review article

https://doi.org/10.1038/s41566-024-01391-5

In vivo NIR-II fluorescence imaging for biology and medicine

Received: 17 September 2023

Accepted: 8 January 2024

Published online: 04 March 2024



Check for updates

Feifei Wang 1, Yeteng Zhong 2, Oliver Bruns, Yongye Liang & Hongjie Dai © 6,7 🖂

Owing to reduced light scattering and tissue autofluorescence, in vivo fluorescence imaging in the 1,000–3,000-nm near-infrared II (NIR-II) spectral range can afford non-invasive imaging at depths of millimetres within biological tissue. Infrared fluorescent probes labelled with antibodies or other targeting ligands also enable NIR-II molecular imaging at the single-cell level. Here we present recent developments in the design of fluorophores and probes emitting in the NIR-II window based on organic synthesis and nanoscience approaches. We also review advances in NIR-II wide-field and microscopy imaging modalities, with a focus on preclinical imaging and promising clinical translation case studies. Finally, we outline current issues and challenges for the wider adoption of NIR-II imaging in biomedical research and clinical imaging.

Optical imaging is important to biology and medicine as it offers exceptional spatiotemporal resolution for non-invasive in vivo imaging, with potentially diffraction-limited or sub-diffraction-limited spatial resolution in real time, and it therefore complements X-ray computed tomography, magnetic resonance imaging and ultrasound imaging. However, the spatial resolution and penetration depth of in vivo fluorescence imaging into live tissues is limited by the combined effects of absorption, scattering, tissue autofluorescence, the quantum yields (QYs) of probes, the optical configuration and detector sensitivity/efficiency. High-resolution fluorescence imaging relies on ballistic and slightly scattered snake-like photons transmitting through tissues, whereas multiple-scattered diffusive photons contribute to noise or background and worsen the diffraction-limited resolution^{1,2}. Light scattering within tissues is dominated by Rayleigh and Mie scattering³, both of which decrease at longer wavelengths as $\lambda^{-\alpha}$ (ref. 4; Fig. 1a), where λ is the imaging wavelength and $\alpha = 0.2-4$ for tissues⁵. Reduced light scattering can afford deeper and higher-contrast fluorescence imaging with less diffusive noise at longer wavelengths.

For decades, near-infrared imaging in the 700–900-nm NIR-I window has been pursued for in vivo biomedical imaging⁶ so as to benefit from the suppressed light scattering by tissues compared to visible light as well as lower absorption by haemoglobin⁷. NIR-I fluorescence imaging became widely accepted as a result of the successes of fluorophores such as indocyanine green (ICG) and the advent of digital imaging technology in the early 2000s8. However, in vivo imaging in NIR-I still suffers from feature blurring caused by light scattering, shallow penetration depth and a high background due to both scattering and autofluorescence from endogenous chromophores or pigmented components in the body^{9,10}.

The Dai group, in 2009, demonstrated the first 1,000-1,700-nm NIR-II preclinical fluorescence imaging of mice using hydrophilic-polymer-coated single-walled carbon nanotubes (SWNTs) and a liquid-nitrogen-cooled indium gallium arsenide (InGaAs) camera¹¹. In 2022, the group performed in vivo imaging in the 1,700-2,000-nm range and refined the definition of NIR-II to 1,000-3,000 nm (ref. 12), largely overlapping with the 900-3,000-nm short-wave infrared (SWIR) range. Subsequently, the group further improved the

Department of Electrical and Electronic Engineering, The University of Hong Kong, Hong Kong, China. 2CAS Key Laboratory for Biomedical Effects of Nanomaterials and Nanosafety, CAS Center for Excellence in Nanoscience, National Center for Nanoscience and Technology, Chinese Academy of Sciences, Beijing, China. 3Department for Functional Imaging in Surgical Oncology, National Center for Tumor Diseases (NCT/UCC) Dresden, Dresden, Germany. ⁴Helmholtz Pioneer Campus, Helmholtz Zentrum München, Neuherberg, Germany. ⁵Department of Materials Science and Engineering, South University of Science and Technology of China, Shenzhen, China. Bepartment of Chemistry and Bio-X, Stanford University, Stanford, CA, USA. ⁷Department of Chemistry, Department of Mechanical Engineering and School of Biomedical Sciences, The University of Hong Kong, Hong Kong, China. ≥e-mail: hdai@stanford.edu

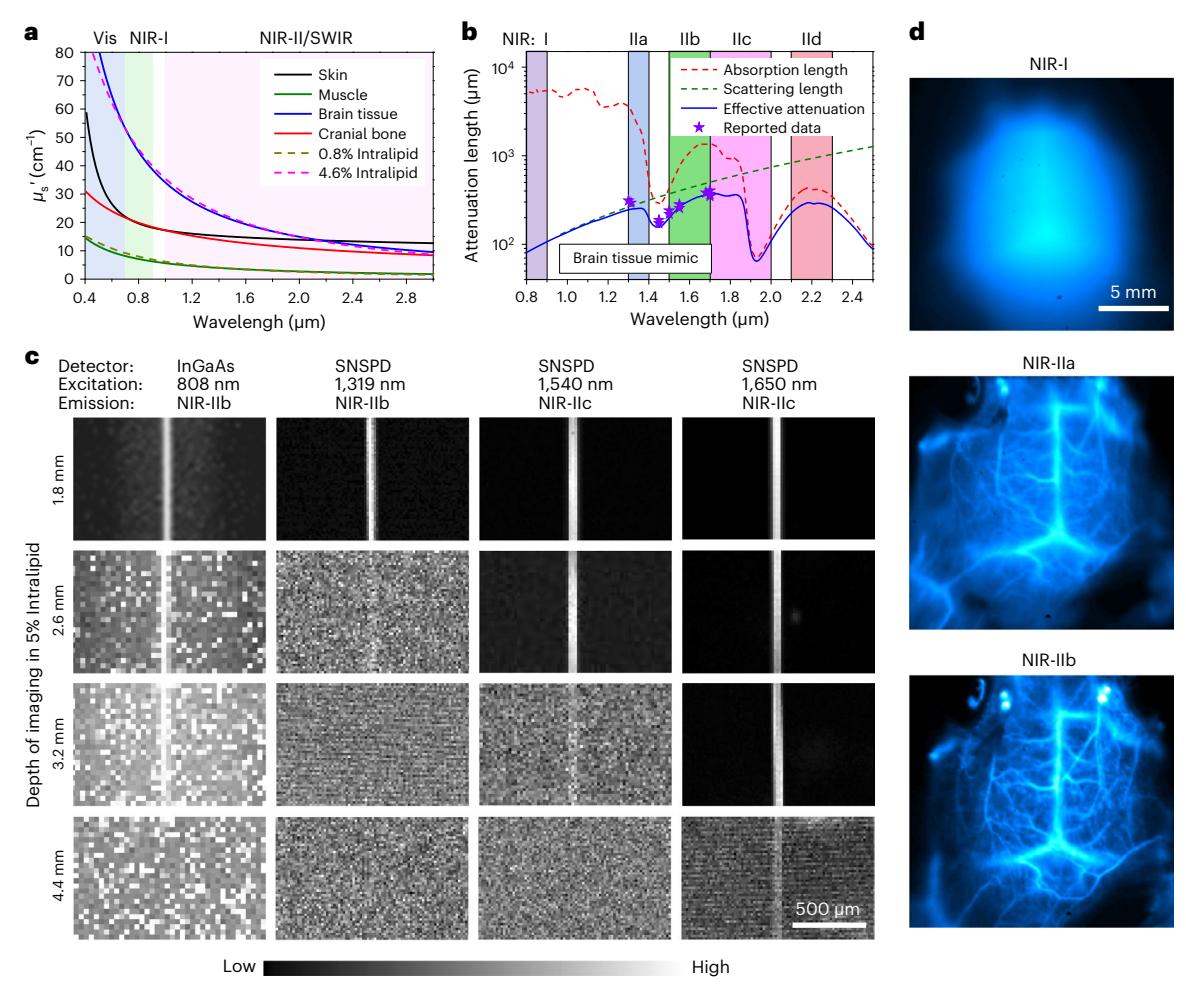


Fig. 1 | **Motivation for NIR-II fluorescence imaging. a**, Reduced scattering coefficients of different biological tissues and the Intralipid phantom with concentrations of 0.8% and 4.6% in the 400–3,000-nm window. **b**, The attenuation length $(1/(1/l_s+1/l_a))$ of brain tissue mimicked by 5% Intralipid solution in the NIR-I and NIR-II windows, where l_s and l_a are the scatter and attenuation lengths, respectively 12 . The stars in the graph denote the effective attenuation lengths of mouse brain that have been reported previously 78,119 . **c**, Fluorescence imaging of a 50-μm capillary submerged at various depths

in 5% Intralipid by a wide-field system with a 2D InGaAs camera or a confocal microscope with SNSPDs. An 808-nm and a 1,319-nm laser were used for NIR-Ilb wide-field imaging and confocal microscopy, respectively. NIR-Ilc confocal microscopy was performed with 1,540-nm or 1,650-nm excitation $^{12}.\,$ **d**, Noninvasive NIR-I, NIR-Ila and NIR-Ilb fluorescence imaging of cerebral vasculatures of mice $^{17}.\,$ Credit: panels $\bf b$ and $\bf c$ adapted with permission from ref. 12, Springer Nature Ltd. Panel $\bf d$ reproduced with permission from ref. 17, Wiley.

imaging spatial resolution, imaging depth and signal/background ratio (SBR) and diminished tissue autofluorescence with NIR-II over NIR-I imaging^{5,10-29}. Light absorption by water in biological tissues and light scattering by tissues limit the penetration depth of light into a living body. Given water absorption by vibrational overtone modes, tissue scattering of light and the detection range of ~900-1,700 nm of InGaAs cameras, one can divide the NIR-II range into several sub-windows with local maxima in light penetration depth versus wavelength (Fig. 1b)12; these sub-windows include the NIR-IIa (1,300-1,400 nm), NIR-IIb (1,500-1,700 nm), NIR-IIc (1,700-2,000 nm) and NIR-IId (~2,100–2,300 nm) windows. Moderate light absorption by water in the 1,400-1,500-nm range was shown to enhance NIR-II image contrast due to the fact that multiply-scattered diffusive light decays faster than ballistic light^{30,31}. Beyond NIR-IId, light absorption by the vibrational normal modes of water is too strong, making through-tissue fluorescence imaging impossible¹². Fluorescence imaging of a fluorophore-filled capillary through different thicknesses of tissue phantoms made of Intralipid solutions (Fig. 1c)¹² and mouse brain (Fig. 1d)¹⁷ showed clearly improved resolution and SBR when transitioning from NIR-I and IIa to the IIb and IIc sub-windows. This is because high resolution and low feature smearing hinge on low scattering, which is provided with

longer-wavelength light. NIR-II imaging beyond a tissue depth of 1 cm has also been demonstrated 32.

Notably, although NIR-I light exhibits much lower light absorption, its tissue penetration depth is much shallower than for NIR-II light due to scattering (Fig. 1b), making NIR-II imaging a step-out technology over the traditional NIR technique. The large Stokes shift between excitation (typically 808 nm) and emission for wide-field imaging in the >1,500-nm NIR-IIb, IIc and IId sub-windows eliminates any tissue autofluorescence background (Fig. 1d), even in mouse liver¹⁰. The NIR-IIb and IIc regions are the highest-performing sub-windows for in vivo NIR-II imaging.

Recent progress in NIR-II fluorophores and nanoprobes

Fluorescent probes for biological imaging should exhibit high brightness (high quantum yield (QY)) and molar absorptivity/extinction coefficient) and biocompatibility. The QY of NIR-II fluorophores is lower than those for their visible or NIR-I counterparts. In molecular fluorophores, non-radiative relaxation between the zero-vibrational level of excited states and the higher isoenergetic vibrational levels of the ground state can quench molecular fluorescence³³, and this effect,

called the 'energy gap law', becomes more pronounced as the energy gap shrinks at longer wavelengths. In aqueous environments, the NIR-II molecular fluorophores, typically with larger π -conjugated backbones, suffer from stronger intermolecular interactions, which lead to further non-radiative decay of the NIR-II emission³⁴. The abundance of hydroxyl groups in aqueous solution is also reported to be a serious quencher of NIR-II luminescence of rare-earth nanoparticles (RENPs)¹⁹. The nonpolar conjugated backbones of molecular fluorophores and the hydrophobic capping layers of inorganic nanoparticles require effective hydrophilic modification for biocompatibility, a process that decreases the fluorescence QY drastically. Despite these challenges, recent years have witnessed an outpouring of promising high-performance NIR-II probes.

Inorganic nanostructured NIR-II probes

The first NIR-II imaging 11 utilized photoluminescent SWNTs in the 1,000-1,700-nm range (Fig. 2a)13, depending on the nanotube chirality and diameter (0.7-1.4 nm; Fig. 2b)^{5,15,17,35}. NIR-II quantum dots (QDs) such as silver sulfide (Ag₂S; 1,100-1,400 nm)^{16,36}, lead sulfide (PbS; 1,000-2,000 nm; QDb: 1,500-1,700 nm and QDc: 1,700-2,000 nm; Fig. 2c)^{12,21} and indium arsenide (InAs; 900–1,600 nm; Fig. 2d)³⁷ were shown to exhibit a higher fluorescence QY than SWNTs. These QDs were typically overcoated with a passivation shell to avoid oxidation, affording core-shell QDs with bright NIR-II emission in aqueous solutions^{12,21,37}. Downconversion RENPs have shown fascinating optical properties, such as narrowband emission spanning the NIR-II range³⁹, long luminescence lifetimes (on the scale of up to tens of milliseconds) 40 and Auger-effect-based persistent luminescence after X-ray irradiation³⁸. To enhance the NIR-II emission, Ce³⁺-doping¹⁹ and cubic-phase²³ strategies can suppress upconversion while boosting Er³⁺ downconversion luminescence at 1,550 nm by approximately nine- and eightfold, respectively. More recently, cubic-phase RENPs based on a Tm³⁺ emitter have been developed (Fig. 2e) that exhibit 1,600-1,700-nm sub-NIR-IIb fluorescence amplification⁴¹. Finally, gold molecular clusters with ultrasmall size (Au₂₅, ~1.6 nm; Fig. 2f) exhibited luminescence in the 1,000-1,400-nm range^{27,42,43}.

Inorganic nanostructured NIR-II probes are often synthesized in organic solvents and coated with hydrophilic, crosslinked polymer layers ('P³ coating'; Fig. 2g) to impart high biocompatibility for preclinical use^{23,25}. The P³ crosslinked surface coating enables rapid biliary clearance and reduces long-term retention-induced side effects of a wide range of nanomaterials, including RENPs, PbS QDs and superparamagnetic iron-oxide nanoparticles, enhancing their in vivo pharmacokinetics and their potential use for nanomedicine²⁵.

Molecular fluorophores

Molecular fluorophores are important NIR-II probes owing to their well-defined structures, rich chemical and structural tunability and generally high biocompatibility and favourable pharmacokinetics. Thus far, NIR-II molecular fluorophores include polymethine (Fig. 2h)^{44,45}, donor–acceptor molecules (Fig. 2i)^{18,46,47}, boron-dipyrromethene (BODIPY; Fig. 2j)⁴⁸, rhodamine (Fig. 2k)⁴⁹ and metal–macrocycles complexes (Fig. 2l)⁵⁰. High-performance in vivo NIR-II fluorescence imaging has been demonstrated using organic fluorophores exhibiting advanced properties such as a long-wavelength peak absorption up to 1,400 nm (ref. 45), large absorption coefficient of 10⁵ mol⁻¹ cm⁻¹ (ref. 51), high QYs of >5% (ref. 47) or long emission in the NIR-IIb window⁵². These molecules generally have large conjugated backbones with high hydrophobicity. For aqueous solubility, researchers typically encapsulate the molecules in amphiphilic polymer matrices^{21,53} or functionalize them with hydrophilic side chains⁵⁴.

The absorption/emission wavelength of NIR-II molecular fluorophores can be redshifted by increasing the conjugated backbone length⁵², increasing the donor/acceptor unit strength⁵⁵ or forming J-aggregates⁴⁵. Video-rate multicolour imaging with NIR-II fluorescence under a multiplexed excitation wavelength has been demonstrated

with flavylium polymethine dyes with finely tuned heterocycle modification⁴⁴. Owing to the energy gap law, redshifted fluorophores generally show lower QYs, especially for molecular fluorophores with peak absorption over 1,000 nm. Strong interactions between water molecules and conjugated backbones cause substantial non-radiative decay for NIR-II molecular fluorophores^{54,55}. Protecting the conjugated backbones from water molecules is thus vital for high fluorescent QYs under aqueous conditions.

An advantage of organic NIR-II fluorophores over inorganic nanoparticle probes is their smaller size, which favours renal excretion upon administration to a body. Renal excretion of NIR-II probes is preferred when considering potential clinical use, because excretion through the kidney/urinary pathway is fast, making them safer and less likely to cause toxic effects than probes remaining in the body for extended times. So far, only a few NIR-II molecular fluorophores have been reported with renal-excretion ability 18,20,48,56 . A caveat is that attaching highly hydrophilic side groups such as β -cyclodextrin $(\beta\text{-CD})^{56}$ and poly(oligo(ethylene glycol) dimethacrylate) polymer brushes 48 to NIR-II fluorophores can facilitate renal excretion, but this typically lowers the fluorescence QY due to non-radiative relaxation of excited states by strong fluorophore—water interactions.

Fluorescent proteins

Genetically encoded fluorescent proteins (FPs) have been widely deployed for long-term visualization and tracking of molecules, cells or structures with high specificity in cells or organisms. Recently, there has been growing interest in the emission tails of NIR-I FPs into the >1,000-nm NIR-II window, thanks to their ability to achieve reduced light scattering, improved imaging depth/resolution and reduced diffused noise⁵⁷. Bacterial phytochrome photoreceptors (BphPs), cyanobacteriochromes (CBCRs) and allophycocyanins (APCs) have been employed as a source to design NIR-IFPs⁵⁸. It has been demonstrated that FPs engineered from BphPs (for example, iRFP670, iRFP682, iRFP702, iRFP713 and iRFP720)⁵⁹ and CBCRs (for example, monomeric miRFP670nano and miRFP718nano)⁶⁰ exhibit fluorescence emission tails in the NIR-II window. iRFP713 has been knocked into the mouse genome for long-term monitoring of liver regeneration models and imaged at >900 nm (ref. 59). The NIR-II fluorescence of miRFP718nano was three times brighter than miRFP670nano and 1.5- and two times brighter than the fluorescence of miRFP709 and miRFP703, respectively⁶⁰. The performance of miRFP718nano has been evaluated for liver inflammation models beyond 1,050 nm, using 50 mW cm^{-2} excitation and a 30 -ms exposure time⁶⁰.

NIR-II imaging modalities

NIR-II 2D wide-field imaging

NIR-II wide-field fluorescence imaging employs an excitation source such as an expanded laser beam¹¹, a light-emitting diode (LED)²³, an X-ray beam⁶¹ or Cerenkov radiation⁶² (Fig. 3a) to illuminate an entire 3D object (for example, a mouse), and projects the generated NIR-II fluorescence to a 2D image captured by a camera. Non-coaxial excitation is commonly employed to avoid the use of dichroic mirrors and background signals due to intense reflections from the samples. Other NIR-II wide-field modes requires no excitation source, including chemiluminescence⁶³, bioluminescence⁶⁴ and afterglow fluorescence imaging³⁸. Wide-field imaging of phantoms or tissues has shown NIR-II imaging penetration depths and resolutions that are -1.7 (refs. 5,17,32,59,64–66) and -2.1 (refs. 15,17,66–69) times better than NIR-I imaging, respectively, though these are significantly influenced by the imaging conditions.

NIR-II imaging in various sub-windows requires a suitable camera and optical filters on the imaging side. For NIR-IIa and NIR-IIb fluorescence imaging, a cooled InGaAs camera (900–1,700 nm) with wide dynamic range and low read noise and dark current is used. For NIR-IIc and NIR-IId wide-field imaging, cameras based on photosensitive semiconductors with small bandgaps, such as 'extended InGaAs' (900–2,600 nm), indium antimonide (InSb, 960–5,000 nm) and mercury

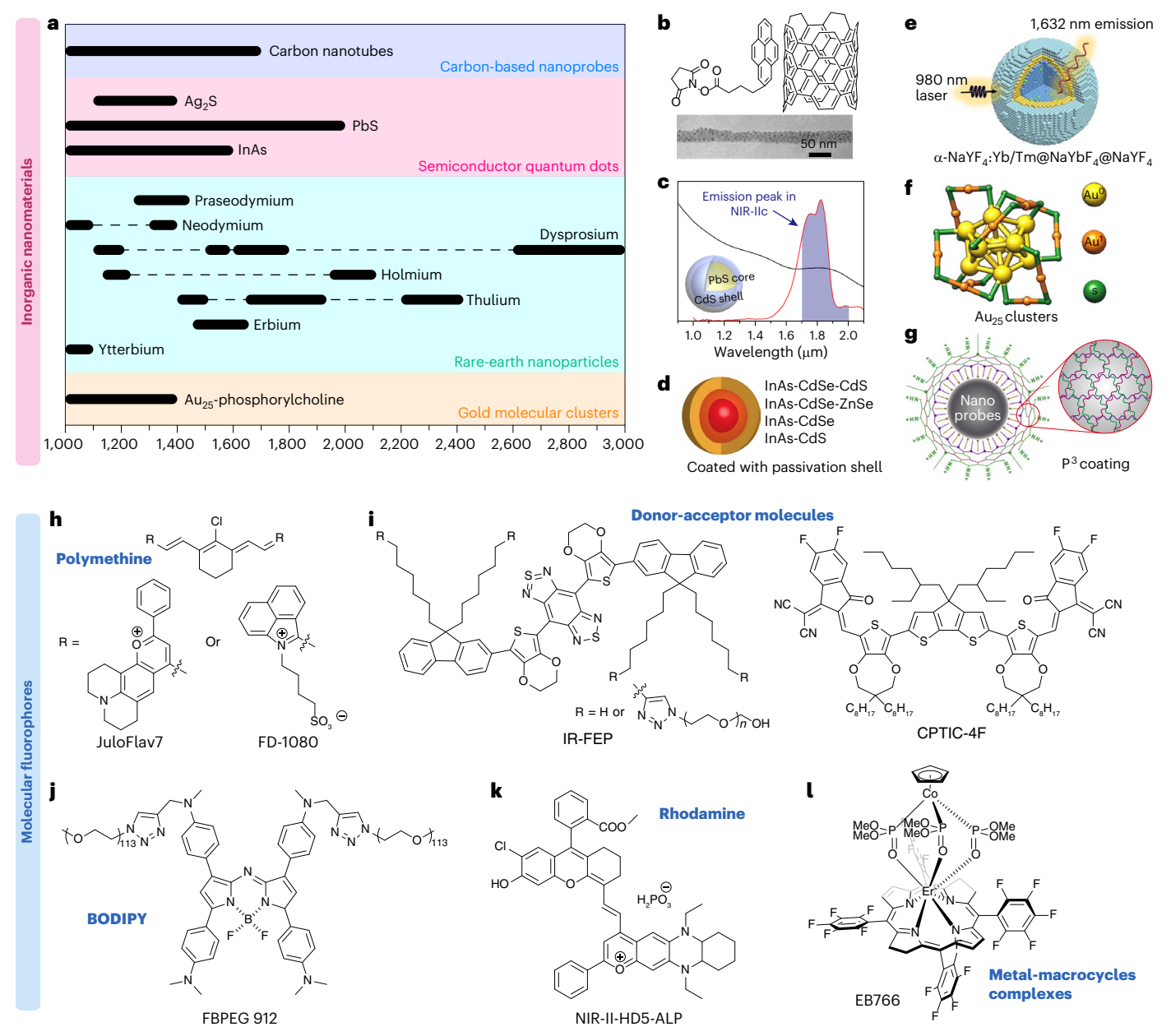
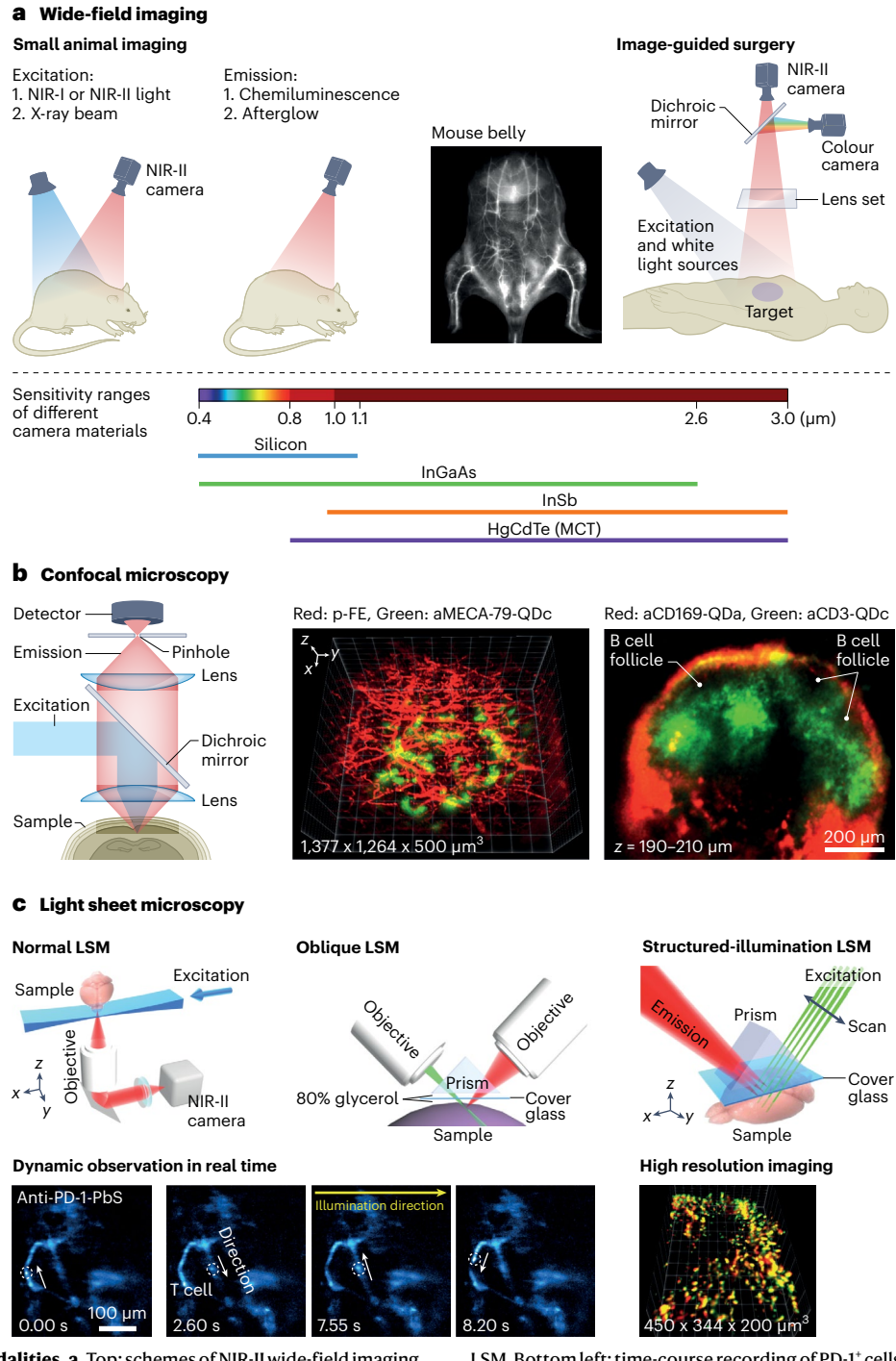


Fig. 2 | **NIR-II fluorescence probes. a**, Emission spectral ranges of different inorganic nanostructured NIR-II probes. **b**, Schemes of SWNTs with proteins anchored on the surface via pyrene π-stacking³⁵. **c**, Emission spectrum and schematic design (inset) of NIR-IIc core–shell PbS/CdS QDs¹². **d**, Schematic overview of InAs-based QDs coated with a passivation shell³⁷. **e**, Schematic of the Tm³⁺-doped cubic-phase core–shell-structured RENPs⁴¹. **f**, Crystallographic representation of Au₂₅ nanoclusters²⁷. **g**, Schematic illustration of the hydrophilic RENPs with P³ coating crosslinking polymeric layers²³. **h–1**, Example structures of the NIR-II molecular fluorophores polymethine (JuloFlav7⁴⁴ and FD-1080⁴⁵; **h**), donor–acceptor molecules (IR-FEP⁴⁶ and CPTIC-4F⁴⁷; **i**), BODIPY (FBPEG 912⁴⁸; **j**), rhodamine (NIR-II-HD5-ALP⁴⁹; **k**) and metal–macrocycles complexes (EB766⁵⁰; **I**). Credit: panel **b** adapted with permission from ref. 35, American

Chemical Society. Panel **c** reproduced with permission from ref. 12, Springer Nature Ltd. Panel **d** adapted with permission from ref. 37, Springer Nature Ltd. Panel **e** reproduced with permission from ref. 41, Springer Nature Ltd. Panel **f** adapted from ref. 27 under a Creative Commons licence CC BY 4.0. Panel **g** adapted with permission from ref. 23, Springer Nature Ltd. Panel **h** (left) adapted with permission from ref. 44, Springer Nature Ltd. Panel **h** (right) adapted with permission from ref. 45, American Chemical Society. Panel **i** (left) adapted with permission from ref. 46, Wiley. Panel **i** (right) adapted with permission from ref. 47, Springer Nature Ltd. Panel **j** adapted with permission from ref. 48, Wiley. Panel **k** adapted with permission from ref. 50, Springer Nature Ltd.

cadmium telluride (HgCdTe or MCT, 800–14,000 nm) are required. Recently, NIR-IIc wide-field imaging was explored utilizing an MCT camera 70 , but this has higher cost, higher noise and lower sensitivity than the commonly used InGaAs cameras. The NIR-II wide-field imaging acquisition speed has reached 300 fps (frames per second) using a fast InGaAs camera 71 . The resolution of NIR-II wide-field imaging with a field of view covering the entire mouse is ~100 μm , limited by the small numbers of pixels of available cameras.

For NIR-II imaging-guided surgery, a multispectral system is essential, allowing concurrent visible photographic and NIR-II fluorescence/luminescence imaging under bright surgical-room light conditions (Fig. 3a). To avoid imaging parallax, the colour camera and NIR-II camera could share the same chromatic aberration-corrected lens set²⁸ or use two separate lens sets sharing a portion of the same coaxial optical path⁷², allowing both cameras to capture the same location from the same angle.



 $\label{eq:Fig. 3} \ | \ NIR-II \ imaging \ modalities. \ a, \ Top: \ schemes of \ NIR-II \ wide-field \ imaging \ systems for \ small-animal \ imaging \ and \ image-guided \ surgery. \ Bottom: \ sensitivity \ range of the \ different \ camera \ materials. \ b, \ Left: \ scheme \ for \ the \ NIR-II \ confocal \ microscope. \ Middle: \ non-invasive \ confocal \ microscopy \ of \ blood \ vessels \ (red) \ in the \ NIR-II \ window \ and \ HEVs \ labelled \ by \ aMECA-79-QDc \ (green, \ QDc: \ NIR-IIc \ PbS \ QDs) \ in the \ NIR-II \ window \ in \ an \ inguinal \ LN. \ Right: \ confocal \ microscopy \ of \ CD169^+ \ macrophages \ (aCD169-QDa, \ QDa: \ NIR-II \ aPbS \ QDs) \ and \ CD3^+ \ T \ cells \ (aCD3-QDc) \ in \ an \ inguinal \ LN^{12}. \ c, \ Top: \ schemes \ of \ NIR-II \ light \ sheet \ microscopes \ with \ normal \ and \ oblique \ configurations \ and \ NIR-II \ structured-illumination$

LSM. Bottom left: time-course recording of PD-1 $^{+}$ cells (white circles) in a CT26 tumour labelled by anti-PD-1-PbS QDs, at 20 frames per second using oblique LSM 24 . Bottom right: a higher-resolution NIR-II structured-illumination LSM of aCD4-ErNPs (red) and aOX40-QDb (green) in a CpG-treated tumour 26 . Credit: panel $\bf b$ (middle, right) reproduced with permission from ref. 12, Springer Nature Ltd. Panel $\bf c$ (bottom left) adapted with permission from ref. 24, Springer Nature Ltd. Panel $\bf c$ (bottom right) reproduced with permission from ref. 26, National Academy of Sciences.

NIR-II 3D confocal microscopy

NIR-II confocal microscopy employs a laser beam tightly focused to a point raster scanned in x-y-z to excite fluorophores, point by point, in a sample. At each point the emitted fluorescence is detected after passing through a pinhole to reject out-of-focus signals, and the signal

is used to construct a three-dimensional (3D) image (Fig. 3b). Confocal NIR-II fluorescence imaging increases the tissue penetration depth limit by approximately tenfold compared with visible confocal microscopy (<100 μm in the visible). The penetration depth of confocal microscopy can be optimized by employing both long excitation and emission

wavelengths, high-QY fluorophores and detectors with high sensitivity and low noise.

Initially, NIR-II confocal microscopy was realized by using NIR-I excitation, NIR-II emission and an InGaAs photomultiplier tube (PMT) detector^{21,73}. For example, NIR-IIb confocal imaging of QDb in mouse blood vasculature under 785-nm excitation resolved blood vessels at -700 µm in intact tumours on mice with sub-10-µm resolution²¹. Confocal imaging of aggregation-induced emission (AIE) dots-filled cerebral blood vessels after craniotomy was performed using 793-nm excitation and >1,000 nm emission, and achieved an 800-µm penetration depth in mouse brain with -9-µm resolution⁷⁴. Recently, we exploited a superconducting nanowire single-photon detector (SNSPD) for NIR-II confocal microscopy and found it superior to InGaAs PMTs, with shorter timing jitter, higher sensitivity and lower noise¹². A home-built SNSPD with a timing jitter of -109 ps was employed for NIR-II lifetime imaging using an 800-nm femtosecond laser for excitation⁷⁵.

NIR-II confocal microscopy with 1,310-nm excitation, QDb probes and an SNSPD enabled the imaging of cerebral blood vessels in vivo at a depth of ~1.7 mm into the hippocampus region after craniotomy 76, close to the ~1.6-mm imaging depth achieved by 1,280-nm-excited two-photon microscopy⁷⁷. The tunable spectrum-response range of SNSPDs presents opportunities for confocal imaging in the NIR-IIc and NIR-IId windows, beyond the detection limit of InGaAs PMTs. To push the penetration depth limit of in vivo non-invasive one-photon imaging, NIR-IIc confocal microscopy with 1,650-nm excitation was demonstrated using QDc and an SNSPD, achieving an imaging depth of ~1.1 mm into an intact mouse head. It also allowed non-invasive through-tissue molecular imaging of mouse inguinal lymph nodes (LNs) with single-cell and single-vessel resolution (Fig. 3b, middle and right)12. This was the first time that both excitation and emitted light in the >1,500-nm regime were utilized for in vivo confocal imaging to minimize light scattering and maximize imaging depth.

The longest excitation wavelength of 1,650 nm for NIR-II one-photon confocal microscopy is close to that (~1,700 nm) used for multiphoton microscopy⁷⁸, with the excitation light intensity decaying similarly upon travelling through tissues. One-photon fluorescence emission of the excited probes scales linearly with excitation light intensity, whereas two-photon and three-photon fluorescence scale with the second and third power of the excitation, respectively^{12,79}. This suggests a slower emission intensity decay and deeper imaging depth of confocal microscopy than multiphoton microcopy with a similar excitation wavelength. In vivo NIR-IIc confocal microscopy can be conducted non-invasively through intact tissues, in contrast to multiphoton intravital microscopy. Multiphoton imaging is advantageous in terms of its higher SBR⁷⁹ and the availability of genetically engineered probes. By combining NIR-IIc confocal microscopy with multiphoton microscopy, both of which use ~1,650-1,700-nm excitation, one could maximize the capability of multichannel molecular-specific and cellular-specific imaging to investigate complex biological systems in vivo.

NIR-II 3D light sheet microscopy

Light sheet microscopy (LSM) utilizes orthogonally arranged illumination and wide-field detection to afford high-speed optical sectioning and 3D volumetric imaging. This approach minimizes phototoxicity and improves subcellular resolution 80 and enables sub-diffraction-limited resolution by using lattice illumination and adaptive optics 81 . However, the imaging depth of LSM for in vivo imaging of live tissues in the visible window is shallow (-200 μm for mouse brain after craniotomy 24) due to light scattering. Two-photon LSM at 1,040 nm allows for deeper imaging into mouse brain (up to -300 μm), with high resolution, due to reduced scattering of the NIR-II excitation 82 . The penetration depth can be further extended by using a Bessel 83 or Airy beam 84 for excitation, but this is still limited by scattering of the visible emitted light.

An oblique NIR-IIb LSM with ~1,319-nm excitation and ~1,500–1,700-nm detection was developed for in vivo mice imaging with cellular resolution 24 (Fig. 3c, middle). This NIR-II LSM avoided the shadows and stripes caused by tissue scattering and absorption, problems common to visible LSM. NIR-IIb LSM enabled non-invasive imaging/sectioning of an intact mouse head with a total penetration depth of ~750 μm , resolving vascular channels connecting the skull and brain cortex of mice. These channels are used by immune cells trafficking between the skull bone marrow and cortex for immune protection of the mouse brain 85 . In another application, PD-1 $^+$ cells migrating irregularly in tumour vasculatures were monitored by NIR-IIb LSM at a frame rate of 20 fps (Fig. 3c, bottom left).

The wavelength of NIR-II light is two to four times longer than that of visible light, and the diffraction-limited spatial resolution (Rayleigh criterion 86 , 0.61λ /NA) of NIR-II LSM is lower than that of visible LSM. In addition, NIR-II imaging of deep tissues still experiences light scattering, causing an increase in background and reducing spatial resolution. A scanning Airy beam with self-healing or attenuation-compensation properties 84 has been employed for excitation 87 in NIR-II LSM to improve the SBR, tissue penetration and z-direction resolution.

Structured illumination has also been introduced into NIR-IILSM to improve the spatial resolution by extracting high-frequency details embedded in low-resolution moiré fringes imaged under a scanning Gaussian-beam comb pattern with several shifted phases interest. The NIR-II structured-illumination LSM can minimize background interference, increase the SBR and increase the spatial resolution by up to two times (Fig. 3c, right), and has been utilized for the longitudinal imaging of immune cells in response to immunotherapy in the tumour microenvironment of a mouse model in the resolution can be further enhanced by using objectives with a higher numerical aperture (NA).

Applications in preclinical imaging

NIR-II imaging has been extensively performed preclinically since 2009 for (1) visualizing blood vasculature structures and measuring haemodynamics and perfusion for cardiovascular diseases; (2) LN imaging; (3) molecular imaging; and (4) functional imaging.

Vascular and haemodynamic imaging

The dynamic NIR-II imaging speed for haemodynamics has increased from the initial ~5 fps using SWNT probes⁸⁹ to ~90 fps using ErNPs²³ more recently. Cardiovascular disease models have been investigated by NIR-II imaging using circulating carbon nanotubes⁵, QDs³⁷, AIE nanodots⁹⁰ and gold clusters⁹¹, respectively. Dynamic monitoring of blood perfusion and haemodynamics in individual blood vessels for disease models of peripheral arterial disease (PAD)^{15,89}, middle cerebral artery occlusion (MCAO) stroke⁵ (Fig. 4a) and traumatic brain injury (TBI)⁹² have been performed. Vascular regeneration has been imaged longitudinally with PbS/CdS QDs in the NIR-IIb window in a mouse model of PAD. Blood flow was also imaged with InAs QDs in disordered vasculatures in glioblastoma multiforme tumour to observe the impact of brain tumour growth on cerebral vasculatures (Fig. 4b)³⁷. The tumour, arterial vessels and venous vessels were identified by dynamic contrast-enhanced imaging through principal component analysis (PCA)^{6,18,23,25,38}.

$Lymph\,node\,imaging$

Sentinel LNs are the initial drainage nodes of a primary tumour where cancer metastasis first occurs. Locating the sentinel LNs for biopsy is important for assessing metastatic spread to the LN basin⁹³. NIR-II fluorescence imaging provides accurate localization of LNs and lymphatic vessels, with better contrast and resolution than in the NIR-I window^{25,94,95}. Recently, 'super-stealth' Au-phosphorylcholine (Au-PC) nanocluster probes were developed for imaging the draining LNs of cancer tumours after intratumoral administration, with minimal interference from surrounding tissues in vivo (Fig. 4c)²⁷.

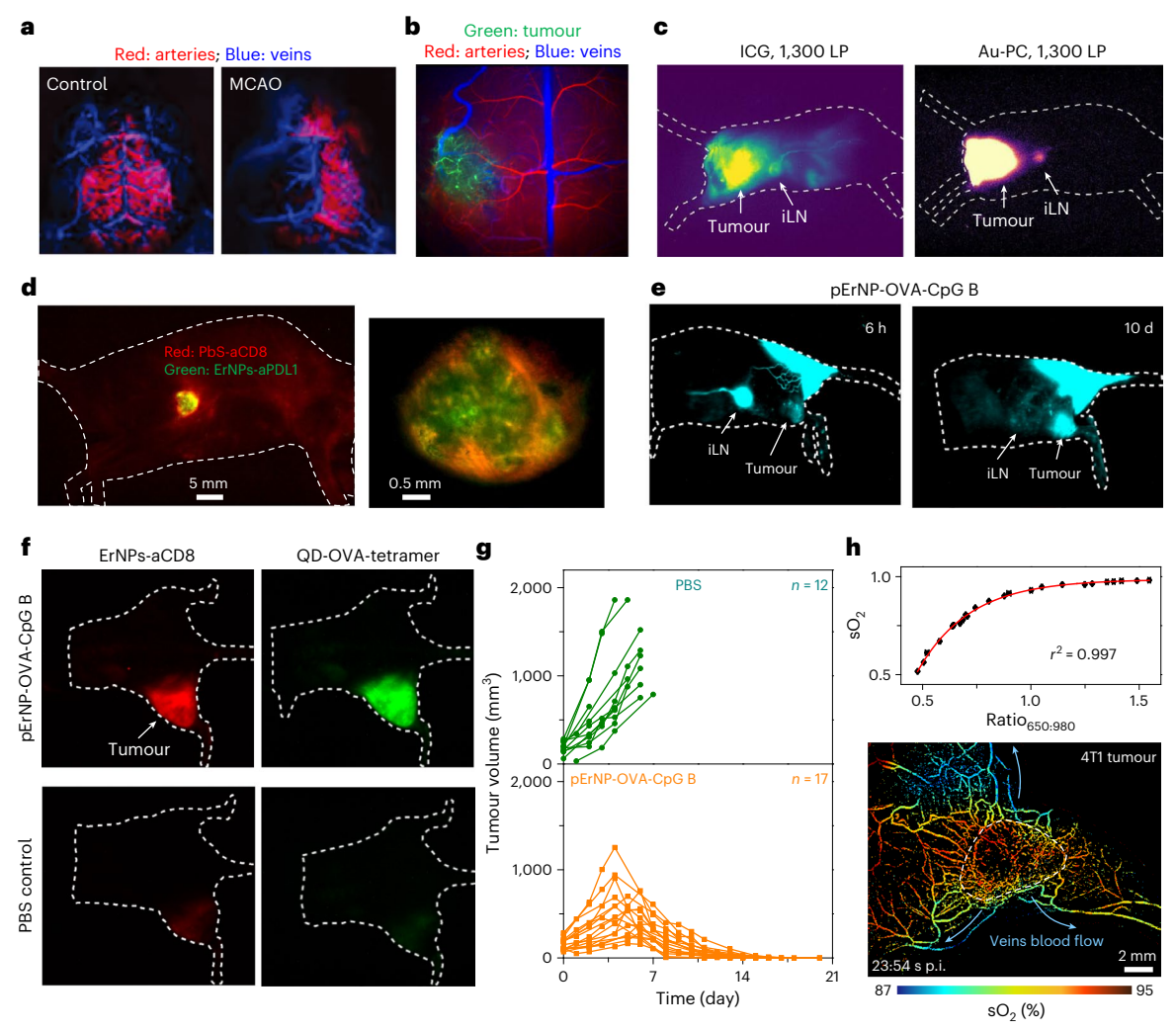


Fig. 4 | **NIR-II preclinical imaging. a**, NIR-II PCA overlaid images showing arterial and venous vessels of a heathy mouse and a mouse with MCAO 5 . **b**, NIR-II imaging of a brain tumour, arteries and veins 37 . **c**, NIR-II imaging of sentinel LNs (inguinal LN, iLN) after injection of ICG and Au-PC 27 . A 1,300-nm longpass filter (1300 LP) was used. **d**, Two-plex NIR-IIb imaging of a mouse bearing a CT-26 tumour at 24 h post intravenous injection of ErNPs-aPDL1 and PbS QDs-aCD8 23 . **e**, Time-course recording of vaccine trafficking pathways after injection of pErNP-OVA—CpG B 29 . **f**, NIR-IIb imaging of mice bearing E.G-7 tumours with intratumoral injection of pErNP-OVA—CpG B or PBS 29 . **g**, Treatment efficacy corresponding to treatment in \mathbf{f}^{e9} .

 ${f h}$, NIR-IIb imaging of sO $_2$. Top: relationship between sO $_2$ value and the ratio of fluorescence signals excited at 650 nm and 980 nm. Bottom: NIR-IIb sO $_2$ imaging of the perfusion of pErNP into a 4T1 tumour 23.54 s post injection (p.i.) 105 . Credit: panel ${f a}$ (left, right) adapted with permission from ref. 5, Springer Nature Ltd. Panel ${f b}$ reproduced with permission from ref. 37, Springer Nature Ltd. Panel ${f c}$ adapted from ref. 27 under a Creative Commons licence CC BY 4.0. Panel ${f d}$ adapted with permission from ref. 23, Springer Nature Ltd. Panels ${f e}$, ${f f}$, ${f g}$ adapted from ref. 29 under a Creative Commons licence CC BY 4.0. Panel ${f h}$ adapted with permission from ref. 105, Springer Nature Ltd.

Molecular imaging

NIR-II molecular imaging of tumour biomarkers has been pursued with targeted NIR-II probes conjugated with antibodies or other ligands, and is capable of high spatial resolution and high contrast differentiation of tumour from normal tissue, with high tumour-to-normal tissue ratios $(T/NT)^{22-29,32}$ in the range of 8–20 in the 1,000–1,400-nm spectral range and up to -40 in the NIR-II window^{23,25,28}, higher than the T/NT = 1.1-4.4 in the NIR-I window^{28,96,97}. Recently, ICG conjugated with bevacizumab has been used to target rat orthotopic colorectal cancer and has been imaged by a white-light and NIR-II endoscopy system⁹⁸.

High endothelial venules (HEVs) in LNs are small postcapillary venules responsible for mediating the entry of immune cells from the blood circulation into LNs 99 . Recently, using targeted antibody-NIR-II probes, in vivo NIR-IIc confocal microscopy has been used to perform non-invasive through-tissue molecular imaging of HEVs, CD169 $^{+}$ subcapsular sinus macrophages and CD3 $^{+}$ T cells in the inguinal LNs of mice (Fig. 3b) 12 .

We employed NIR-II molecular imaging to assess the immune responses of mice to immunotherapy. The different fluorescence lifetimes of ErNPs (-4.6 ms, emission ~1,600 nm) and QDb (-46 μs , emission ~1,600 nm) were exploited for in vivo two-plex NIR-IIb molecular imaging of PD-L1 and CD8, revealing the accumulation of CD8+ cytotoxic lymphocytes (CTLs) in the CT26 tumour following treatment by anti-PD-L1 conjugated to ErNPs (Fig. 4d)^23. Wide-field imaging and structured-illumination LSM were used for multiplex and multiscale molecular imaging of the CT26 tumour microenvironment in mice²6, for longitudinal tracking of CD4, CD8 and OX40 at the single-cell level in response to immunotherapeutic cytosine-phosphate–guanine (CpG) and OX40 antibody treatment by intratumoral injection.

Recently, a cancer nanovaccine was developed by conjugating ovalbumin (OVA) covalently and class-B CpG (CpGB) electrostatically to pErNP 29 . Upon subcutaneous injection, NIR-IIb imaging revealed trafficking of the nanovaccine, rapidly migrating to inguinal LNs (iLN) through the lymphatic vessels (Fig. 4e). Two doses of vaccination led to

tumour eradication and cure/survival of mice. Wide-field imaging and structured-illumination LSM revealed abundant OVA antigen-specific CD8 $^+$ CTLs recruited to the tumour in the treated mouse (Fig. 4f). This was the first time that in vivo imaging of antigen-specific CTLs was performed to correlate with the immunotherapeutic effects of cancer vaccines (Fig. 4g).

NIR-II functional imaging

Functional imaging to probe the environmental parameters and cellular responses to a stimulus is another exciting direction for in vivo NIR-II imaging, with examples including NIR-II fluorescent molecules responding to an external stimulus or environment, such as pH 65 , redox species 100 , nitroreductase 101 , A β plaques 102 and cell endocytosis 103 . A unimolecular NIR-II chemiluminescence probe for H_2S was constructed by conjugating Schaap's dioxetane with a donor–acceptor core 104 . A more recent advancement is NIR-IIb imaging of oxyhaemoglobin saturation (sO $_2$) in blood vessels, based on the absorption difference between oxyhaemoglobin and deoxyhaemoglobin at specific excitation wavelengths (650, 808 and 980 nm) of pErNPs, enabling visualization of the sO $_2$ levels in tumour-associated vessels (Fig. 4h) 105 . Atomically precise NIR-II Au $_{22}$ clusters with strong NIR-II fluorescence exhibit potent enzyme-mimetic activities, which is promising for early intervention regarding oxidative stress 43 .

NIR-II imaging-guided surgery

Preclinical NIR-II imaging for intraoperative navigation is an active area of research with potential clinical translations. Surgical removal of tumours (for example, glioblastoma¹⁸, pancreatic tumour¹⁰⁶, colorectal tumour²⁰, ovarian tumour¹⁰⁷ and breast tumour⁹⁴) navigated by NIR-II imaging holds great promise. NIR-IIb molecular imaging of tumours using ErNP-TRC105 targeting tumour vasculature angiogenesis has afforded a tumour-to-muscle signal ratio of up to ~300, allowing high-precision image-guided tumour resection down to the few-cell level²⁸. A recent work has shown successful surgical removal of LNs labelled with QDb, achieving high LN-to-muscle ratios of ~200 (ref. 94). In another work, NIR-II imaging-guided surgery led to complete resection of severe inflammatory bowels and ensured a secure surgical anastomosis by using AIE nanoprobes¹⁰⁸.

Towards clinical imaging

For any successful clinical translation of NIR-II fluorescence imaging, it is imperative to develop contrast agents that are safe for use in humans. Several groups found that traditional NIR-I organic dyes such as ICG and IRDve800CW exhibited emission tails into the NIR-II window 34,109 and can be utilized for NIR-II imaging to benefit from the reduced light scattering and high imaging contrast and resolution. Because ICG is a Food and Drug Administration (FDA)-approved fluorophore, clinical trials of NIR-II imaging with ICG in human patients is of relatively low risk, but requires switching to an InGaAs-based imaging system, which has not gone through rigorous regulatory approval. Along this line, NIR-II fluorescence-guided surgical resection of liver tumours in human patients was successfully performed after intravenous injection of ICG at a dose of 0.5 mg kg⁻¹, demonstrating a higher tumour detection sensitivity and rate than imaging in the NIR-I region (Fig. 5a)%. However, the ICG is a non-targeted probe, and thus gives false positives of tumours as it accumulates in other tissues 96. Active tumour targeting for imaging-guided surgery has clinically tested bioconjugates of IRDye800CW in the NIR-I window34. IRDye800CW conjugates, exhibiting a tail emission beyond 1,000 nm, have potential for the better determination of tumour margins²⁸.

Another promising direction for clinical translation is NIR-II imaging of perfusion. NIR-II imaging of ICG-tagged blood has been used to observe anastomotic vessels and salvaged distal limbs¹¹⁰. It has allowed the observation of skin perforator vessels at the deep fascial level (Fig. 5b) and revascularization (Fig. 5c) before and after flap transplantation,

respectively, with higher contrast, better resolution and a longer duration of observation than with NIR-I imaging 110 .

Clinical trials of SWIR imaging using a label-free approach by exploiting the absorption properties of water have been reported¹¹¹. One example is the otoscope, which uses the negative contrast of the water absorption band at 1,480 nm to detect fluid in the middle ear¹¹¹.

Outlook and future directions

Probes and fluorophores

Currently, organic NIR-II fluorophores with high absorptivity, QY and aqueous solubility, as well as the ability to be excreted renally and conjugated to target ligands, are still rare. Molecules emitting predominantly in the NIR-IIb sub-window are also desired to compete with nanoprobes based on inorganic QDs and rare-earth nanoparticles. Another major challenge is the synthesis of functional NIR-II fluorophores with optical properties sensitive to the environment and stimuli, especially for imaging-based sensing of pH, gas molecules, Ca^{2+} and other ions, and voltages and action potentials across the ion channels of neurons.

The wide emission spectra of NIR-II fluorophores (full-width at half-maximum of ~75-290 nm) have limited multiplexed imag- $\text{ing}^{\text{18-21,27,36,37,42,112}}.$ Multiplexed molecular imaging can be expanded by employing multicolour probes with different narrowband emissions, probes with different excitation wavelengths, and probes with different fluorescence/luminescence lifetimes, all conjugated to molecular-specific ligands to target different molecules in a body. For inorganic-based nanoparticles, it is desirable to have narrow emission widths across the 1,000-2,300-nm range, with little spectral overlapping. Currently, aqueous soluble, biocompatible NIR-IId probes (emission peak at ~2,200 nm) are lacking. Developing NIR-II probes with tunable fluorescence lifetime is another important approach to increase multiplexed molecular imaging²³ in vivo and should be pursued further. Thus far, three-plex NIR-IIb imaging has been realized by combining continuous-wave and lifetime imaging using QDs and rare-earth nanoparticles²⁹.

Developing genetically engineered NIR-II fluorescent proteins has been a daunting challenge so far, but the success of this would mirror the green fluorescent protein (GFP) revolution, and undoubtedly boost the NIR-II field and lead to much broader adoption of this imaging modality by biologists and medical scientists. NIR-II fluorescent proteins exist in nature, and several purple photosynthetic bacteria, including *Blastochloris tepida*, *Blastochloris viridis* and *Halorhodospira halochloris*, possess bacteriochlorophyll *b*-based light-harvesting complexes exhibiting absorption and fluorescence in the NIR-II range¹¹³. Among these, the light-harvesting 1-reaction centre (LH1-RC) complex from *Blastochloris viridis* has been observed to emit fluorescence with a peak in the NIR-II window¹¹³, opening up opportunities for the development of NIR-II fluorescent proteins, but these very large protein complexes are still very difficult to use in genetic labelling strategies in mammalian cells¹¹⁴.

NIR-II imaging devices and methods

New camera technologies with high sensitivity, low noise, a broad spectral range spanning 1,000–2,300 nm and greater pixel numbers are important to enhance NIR-II imaging performance and capability. High-quantum-efficiency image intensifiers in the NIR-II range are needed for time-resolved/ultrafast imaging and for the detection and imaging of weak fluorescence. Better cameras for NIR-IIc and NIR-IId imaging beyond InGaAs are required to optimize the benefit of in vivo fluorescence imaging in 2D wide-field and 3D LSM modes. Point detectors such as SNSPDs have enabled high-resolution, deep-tissue confocal microscopy in the NIR-IIc sub-window, but remain a challenge for the -2,200-nm NIR-IId range, with low dark noise.

To push the resolution limit, it is desirable to introduce optical super-resolution methods to microscopic imaging in the NIR-II window, similar to the approaches developed for the visible range, such

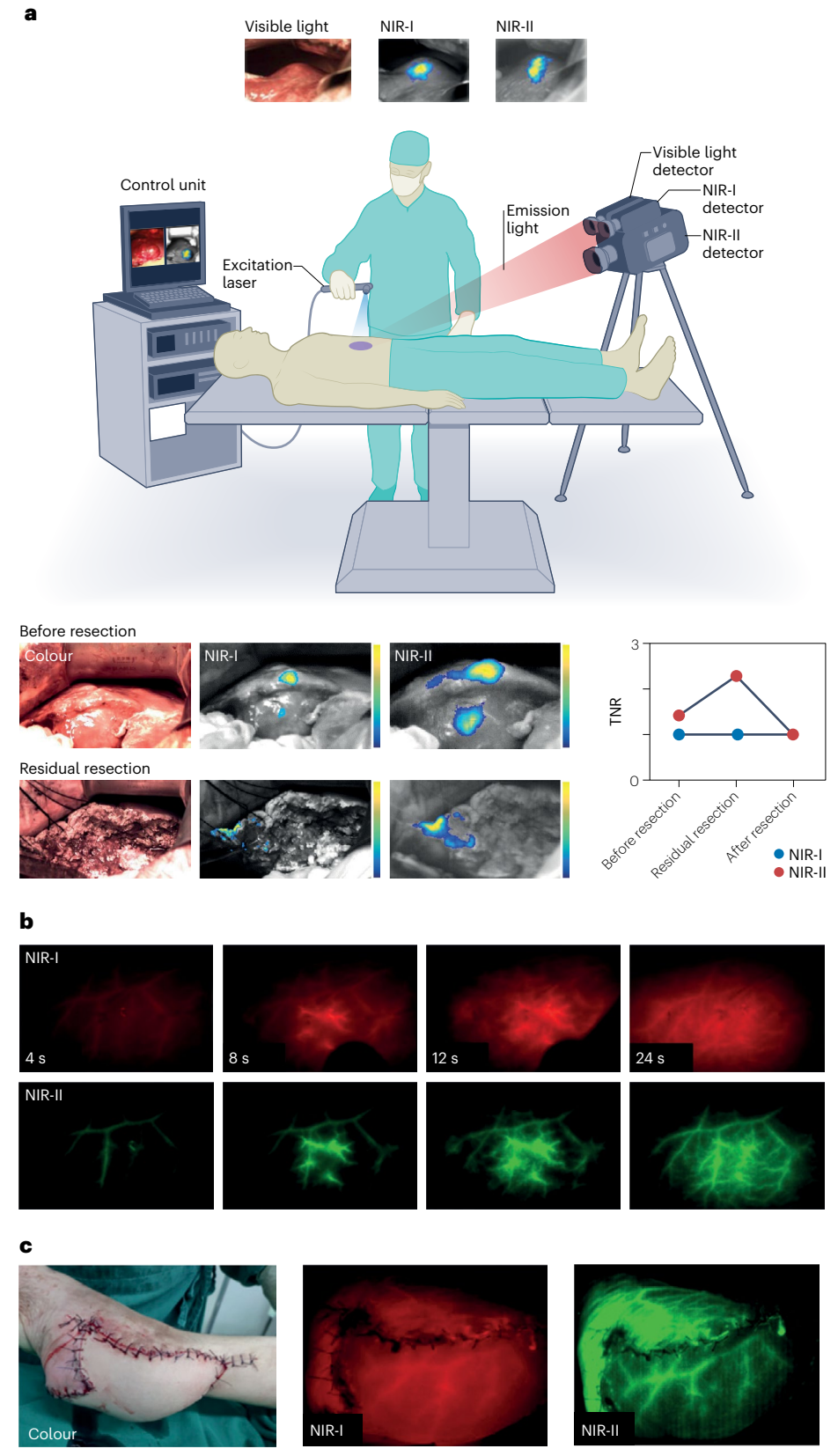


Fig. 5 | **NIR-II clinical imaging. a**, Top: schematic showing example equipment for visible, NIR-I and NIR-II image-guided surgery for clinical tumour resection. Bottom: intraoperative visible, NIR-I and NIR-II imaging of a tumour before and during tumour resection. The tumour-to-normal-tissue ratio (TNR) of NIR-II imaging was higher than that of NIR-I imaging after the first resection, and the TNR of NIR-I and NIR-II imaging became the same after the second resection. **b**, Preoperative NIR-I (top) and NIR-II (bottom) fluorescence imaging, revealing four possible perforators

after intravenous injection of ICG. NIR-II imaging resolved more perforators than the traditional Doppler method. One of them overlapped with the Doppler location 110 . \boldsymbol{c} , Colour image of a human heel after flap transplantation (left), and NIR-I (middle) and NIR-II (right) fluorescence imaging of flap perfusion and revascularization. NIR-II imaging enhances the visualization of revascularization compared to NIR-I imaging 110 . Credit: panel a adapted with permission from ref. 96, Springer Nature Ltd. Panels \boldsymbol{b} and \boldsymbol{c} adapted from ref. 110 under a Creative Commons licence CC BY 4.0.

as nonlinear structured illumination microscopy (SIM), stochastic optical reconstruction microscopy (STORM), photoactivated localization microscopy (PALM) and stimulated emission depletion (STED) microscopy. To realize these, specially designed NIR-II fluorescent probes and low-light-sensitive detectors are required.

An interesting and exciting direction is to use deep learning and artificial intelligence (AI) to enhance NIR-II fluorescence imaging. Recently, the cycle generative adversarial network (CycleGAN) was used to transform a blurred in vivo NIR-I or NIR-IIa image into a much higher-clarity image resembling a NIR-IIb image ¹¹⁵. Training with experimental data in a higher sub-window (for example, NIR-IIc) could be used for machine learning, and then applied to transform and improve images acquired in the lower sub-window (for example, NIR-IIb). AI approaches could address the problems of a scarcity of probes ¹¹⁵ and the affordability of high-end expensive cameras in the higher sub-windows, enabling noise reduction and sensitivity enhancement.

Clinical translation

Preclinical in vivo NIR-II fluorescence imaging has produced a large body of promising results for potential clinical translation. However, a major hurdle is the lack of clinically proven high-performance NIR-II fluorophores or nanoprobes that are safe and have favourable pharmacokinetics for human use. Although the FDA-approved ICG has a high safety track record and exhibits tail fluorescence into the NIR-II window, the emission is mostly in the <1,200-nm range, and imaging still suffers from substantial light scattering and high background. ICG also lacks the functional groups required for conjugation to target ligands and cannot be used for molecular imaging. Alternative dyes or probes are needed that have a safety profile similar to that of ICG, with longer wavelength emission ideally in the NIR-IIb sub-window.

Among the inorganic probes, rare-earth downconversion nanoparticles are bright emitters for the high-performing (low scattering, low autofluorescence) NIR-IIb imaging window, and have afforded excellent molecular imaging agents. Similar-composition upconversion nanoparticles have proven highly safe in mice, preclinically. However, clinical translation is uncertain owing to probe scaling-up issues and the lack of safety data from clinical settings. QDs are even more challenging because of the toxic elements used. Another highly promising NIR-II probe comprises molecular gold clusters such as Au₂₅GSH and Au₂₅PC, as Au is widely accepted to be a safe element, the clusters are rapidly excreted renally, exhibiting little non-specific tissue binding/uptake, and have shown higher performance in NIR-II LN imaging compared to ICG²⁷. Regardless, the clinical translation of any NIR-II agent must undergo rigorous phase I to III clinical trials for pharmacokinetics, toxicity, stability, side effects and risks to humans, and proof of benefits116,117.

Standardization of NIR-II imaging systems is another key step towards clinical translation. A set of characteristics for image devices for clinical use have been suggested to meet the requirements of the operating-room environment and clinical workflow 118. Although originally intended for the evaluation of NIR-I fluorescence-guided surgery systems, these criteria can provide a guide for future clinical NIR-II imaging devices, including (1) the overlay of white-light and fluorescence images in real time, (2) operation within surgical lighting, (3) high sensitivity, (4) in situ quantitative capabilities, (5) concurrent multiplex fluorescence imaging and (6) maximized ergonomic utility for surgery 118. The standardization of NIR-II imagers and contrast agents will accelerate regulatory approval, optimize device development, guarantee product quality, standardize clinical trials and reduce risk 116,117.

The NIR-II imaging has enabled tumour resection down to the few-cell level with zero background 28 . Under this resolution, manual resection/surgical operation by hand could be challenging. We envisage that the combination of NIR-II imaging and surgical robots could become a powerful tool for precision medicine.

References

- Genack, A. Z., Chabanov, A. A., Sebbah, P. & van Tiggelen, B. A. in Encyclopedia of Condensed Matter Physics (eds Bassani, F., Liedl, G. L. & Wyder, P.) 307–317 (Elsevier, 2005).
- Shi, L. & Alfano, R. R. Deep Imaging in Tissue and Biomedical Materials: using Linear and Nonlinear Optical Methods (CRC Press, 2017).
- 3. Jacques, S. L. Optical properties of biological tissues: a review. *Phys. Med. Biol.* **58**, R37–R61 (2013).
- 4. Hong, G., Antaris, A. L. & Dai, H. Near-infrared fluorophores for biomedical imaging. *Nat. Biomed. Eng.* **1**, 0010 (2017).
- 5. Hong, G. et al. Through-skull fluorescence imaging of the brain in a new near-infrared window. *Nat. Photon.* **8**, 723–730 (2014).
- Weissleder, R. A clearer vision for in vivo imaging. Nat. Biotechnol. 19, 316–317 (2001).
- Friebel, M., Helfmann, J., Netz, U. & Meinke, M. Influence of oxygen saturation on the optical scattering properties of human red blood cells in the spectral range 250 to 2,000 nm. *J. Biomed.* Opt. 14, 034001 (2009).
- 8. Reinhart, M. B., Huntington, C. R., Blair, L. J., Heniford, B. T. & Augenstein, V. A. Indocyanine green: historical context, current applications and future considerations. *Surg. Innov.* **23**, 166–175 (2016).
- 9. Smith, A. M., Mancini, M. C. & Nie, S. Second window for in vivo imaging. *Nat. Nanotechnol.* **4**, 710–711 (2009).
- Diao, S. et al. Biological imaging without autofluorescence in the second near-infrared region. Nano Res. 8, 3027–3034 (2015).
- Welsher, K. et al. A route to brightly fluorescent carbon nanotubes for near-infrared imaging in mice. *Nat. Nanotechnol.* 4, 773–780 (2009).
- Wang, F. et al. In vivo non-invasive confocal fluorescence imaging beyond 1,700 nm using superconducting nanowire single-photon detectors. Nat. Nanotechnol. 17, 653–660 (2022).
- 13. Liu, Z., Tabakman, S., Welsher, K. & Dai, H. Carbon nanotubes in biology and medicine: in vitro and in vivo detection, imaging and drug delivery. *Nano Res.* **2**, 85–120 (2009).
- Welsher, K., Sherlock, S. P. & Dai, H. Deep-tissue anatomical imaging of mice using carbon nanotube fluorophores in the second near-infrared window. *Proc. Natl Acad. Sci. USA* 108, 8943–8948 (2011).
- Hong, G. et al. Multifunctional in vivo vascular imaging using near-infrared II fluorescence. Nat. Med. 18, 1841–1846 (2012).
- 16. Hong, G. et al. In vivo fluorescence imaging with Ag_2S quantum dots in the second near-infrared region. *Angew. Chem. Int. Edit.* **51**, 9818–9821 (2012).
- 17. Diao, S. et al. Fluorescence imaging in vivo at wavelengths beyond 1,500nm. *Angew. Chem. Int. Ed.* **54**, 14758–14762 (2015).
- Antaris, A. L. et al. A small-molecule dye for NIR-II imaging. Nat. Mater. 15, 235–242 (2016).
- Zhong, Y. et al. Boosting the down-shifting luminescence of rare-earth nanocrystals for biological imaging beyond 1,500 nm. Nat. Commun. 8, 737 (2017).
- Wan, H. et al. Developing a bright NIR-II fluorophore with fast renal excretion and its application in molecular imaging of immune checkpoint PD-L1. Adv. Funct. Mater. 28, 1804956 (2018).
- Zhang, M. et al. Bright quantum dots emitting at ~1,600 nm in the NIR-IIb window for deep tissue fluorescence imaging. Proc. Natl Acad. Sci. USA 115, 6590–6595 (2018).
- 22. Ma, Z. et al. A theranostic agent for cancer therapy and imaging in the second near-infrared window. *Nano Res.* **12**, 273–279 (2019).
- Zhong, Y. et al. In vivo molecular imaging for immunotherapy using ultra-bright near-infrared-IIb rare-earth nanoparticles. Nat. Biotechnol. 37, 1322–1331 (2019).
- Wang, F. et al. Light-sheet microscopy in the near-infrared II window. Nat. Methods 16, 545–552 (2019).

- Ma, Z. et al. Cross-link-functionalized nanoparticles for rapid excretion in nanotheranostic applications. *Angew. Chem. Int. Ed.* 59, 20552–20560 (2020).
- Wang, F. et al. In vivo NIR-II structured-illumination light-sheet microscopy. Proc. Natl Acad. Sci. USA 118, e2023888118 (2021).
- Baghdasaryan, A. et al. Phosphorylcholine-conjugated gold-molecular clusters improve signal for lymph node NIR-II fluorescence imaging in preclinical cancer models. *Nat.* Commun. 13, 5613 (2022).
- Wang, F. et al. High-precision tumor resection down to few-cell level guided by NIR-IIb molecular fluorescence imaging. Proc. Natl Acad. Sci. USA 119, e2123111119 (2022).
- Ren, F. et al. Shortwave-infrared-light-emitting probes for the in vivo tracking of cancer vaccines and the elicited immune responses. *Nat. Biomed. Eng.* (2023); https://doi.org/10.1038/ s41551-023-01083-5
- Carr, J. A. et al. Absorption by water increases fluorescence image contrast of biological tissue in the shortwave infrared. *Proc. Natl Acad. Sci. USA* 115, 9080–9085 (2018).
- Yoo, K. M., Liu, F. & Alfano, R. R. Imaging through a scattering wall using absorption. Opt. Lett. 16, 1068–1070 (1991).
- Shao, W. et al. Tunable narrow band emissions from dye-sensitized core/shell/shell nanocrystals in the second near-infrared biological window. J. Am. Chem. Soc. 138, 16192–16195 (2016).
- Wei, Y.-C. et al. Overcoming the energy gap law in near-infrared OLEDs by exciton-vibration decoupling. *Nat. Photon.* 14, 570–577 (2020).
- Zhu, S., Tian, R., Antaris, A. L., Chen, X. & Dai, H. Near-infrared-II molecular dyes for cancer imaging and surgery. *Adv. Mater.* 31, 1900321 (2019).
- Chen, R. J., Zhang, Y., Wang, D. & Dai, H. Noncovalent sidewall functionalization of single-walled carbon nanotubes for protein immobilization. J. Am. Chem. Soc. 123, 3838–3839 (2001).
- Zhang, Y. et al. Ag₂S quantum dot: a bright and biocompatible fluorescent nanoprobe in the second near-infrared window. ACS Nano 6, 3695–3702 (2012).
- Bruns, O. T. et al. Next-generation in vivo optical imaging with short-wave infrared quantum dots. *Nat. Biomed. Eng.* 1, 0056 (2017).
- Pei, P. et al. X-ray-activated persistent luminescence nanomaterials for NIR-II imaging. *Nat. Nanotechnol.* 16, 1011–1018 (2021).
- 39. Zhong, Y. & Dai, H. A mini-review on rare-earth down-conversion nanoparticles for NIR-II imaging of biological systems. *Nano Res.* **13**, 1281–1294 (2020).
- 40. Gu, Y. et al. High-sensitivity imaging of time-domain near-infrared light transducer. *Nat. Photon.* **13**, 525–531 (2019).
- Yang, Y. et al. Fluorescence-amplified nanocrystals in the second near-infrared window for in vivo real-time dynamic multiplexed imaging. *Nat. Nanotechnol.* 18, 1195–1204 (2023).
- 42. Chen, Y. et al. Shortwave infrared in vivo imaging with gold nanoclusters. *Nano Lett.* **17**, 6330–6334 (2017).
- Ma, H. et al. Bioactive NIR-II gold clusters for three-dimensional imaging and acute inflammation inhibition. Sci. Adv. 9, eadh7828 (2023).
- 44. Cosco, E. D. et al. Shortwave infrared polymethine fluorophores matched to excitation lasers enable non-invasive, multicolour in vivo imaging in real time. *Nat. Chem.* **12**, 1123–1130 (2020).
- Sun, C. et al. J-aggregates of cyanine dye for NIR-II in vivo dynamic vascular imaging beyond 1,500 nm. J. Am. Chem. Soc. 141, 19221–19225 (2019).
- Yang, Q. et al. Rational design of molecular fluorophores for biological imaging in the NIR-II window. Adv. Mater. 29, 1605497 (2017).

- Zhu, X. et al. High brightness NIR-II nanofluorophores based on fused-ring acceptor molecules. *Nano Res.* 13, 2570–2575 (2020).
- 48. Yao, C. et al. A bright, renal-clearable NIR-II brush macromolecular probe with long blood circulation time for kidney disease bioimaging. *Angew. Chem. Int. Ed.* **61**, e202114273 (2022).
- 49. Qin, Z. et al. NIRII-HDs: a versatile platform for developing activatable NIR-II fluorogenic probes for reliable in vivo analyte sensing. *Angew. Chem. Int. Ed.* **61**, e202201541 (2022).
- Wang, T. et al. A hybrid erbium(III)-bacteriochlorin near-infrared probe for multiplexed biomedical imaging. *Nat. Mater.* 20, 1571–1578 (2021).
- Lei, Z. et al. Stable, wavelength-tunable fluorescent dyes in the NIR-II region for in vivo high-contrast bioimaging and multiplexed biosensing. *Angew. Chem. Int. Ed.* 58, 8166–8171 (2019).
- 52. Liu, S. et al. Incorporation of planar blocks into twisted skeletons: boosting brightness of fluorophores for bioimaging beyond 1,500 nanometer. ACS Nano 14, 14228–14239 (2020).
- Liu, C. et al. 3,4-Ethylenedithio thiophene donor for NIR-II fluorophores with improved quantum yields. *Mater. Chem. Front.* 7, 2419–2425 (2023).
- 54. Ma, H. et al. Propylenedioxy thiophene donor to achieve NIR-II molecular fluorophores with enhanced brightness. *Chem. Mater.* **32**, 2061–2069 (2020).
- 55. Yang, Q. et al. Donor engineering for NIR-II molecular fluorophores with enhanced fluorescent performance. *J. Am. Chem. Soc.* **140**, 1715–1724 (2018).
- Huang, J. et al. Renal-clearable molecular semiconductor for second near-infrared fluorescence imaging of kidney dysfunction. Angew. Chem. Int. Ed. 58, 15120–15127 (2019).
- 57. Shcherbakova, D. M. & Verkhusha, V. V. Near-infrared fluorescent proteins for multicolor in vivo imaging. *Nat. Methods* **10**, 751–754 (2013).
- 58. Oliinyk, O. S., Chernov, K. G. & Verkhusha, V. V. Bacterial phytochromes, cyanobacteriochromes and allophycocyanins as a source of near-infrared fluorescent probes. *Int. J. Mol. Sci.* **18**, 1691 (2017).
- Chen, M. et al. Long-term monitoring of intravital biological processes using fluorescent protein-assisted NIR-II imaging. Nat. Commun. 13, 6643 (2022).
- 60. Oliinyk, O. S. et al. Deep-tissue SWIR imaging using rationally designed small red-shifted near-infrared fluorescent protein. *Nat. Methods* **20**, 70–74 (2023).
- Naczynski, D. J. et al. X-ray-induced shortwave infrared biomedical imaging using rare-earth nanoprobes. *Nano Lett.* 15, 96–102 (2015).
- 62. Cao, X. et al. Cherenkov excited short-wavelength infrared fluorescence imaging in vivo with external beam radiation. *J. Biomed. Opt.* **24**, 051405 (2018).
- 63. Shen, H. et al. Rational design of NIR-II AIEgens with ultrahigh quantum yields for photo- and chemiluminescence imaging. *J. Am. Chem.* Soc. **144**, 15391–15402 (2022).
- 64. Lu, L. et al. NIR-II bioluminescence for in vivo high contrast imaging and in situ ATP-mediated metastases tracing. *Nat. Commun.* **11**, 4192 (2020).
- Wang, S. et al. Anti-quenching NIR-II molecular fluorophores for in vivo high-contrast imaging and pH sensing. *Nat. Commun.* 10, 1058 (2019).
- 66. Starosolski, Z. et al. Indocyanine green fluorescence in second near-infrared (NIR-II) window. *PLoS ONE* **12**, e0187563 (2017).
- 67. Ren, T.-B. et al. A general strategy for development of activatable NIR-II fluorescent probes for in vivo high-contrast bioimaging. Angew. Chem. Int. Ed. **60**, 800–805 (2021).

- Wang, Z. et al. Dynamically monitoring lymphatic and vascular systems in physiological and pathological conditions of a swine model via a portable NIR-II imaging system with ICG. Int. J. Med. Sci. 19, 1864–1874 (2022).
- Xue, D. et al. Structural and functional NIR-II fluorescence bioimaging in urinary system via clinically approved dye methylene blue. *Engineering* 22, 149–158 (2023).
- Chang, Y. et al. Bright Tm³⁺-based downshifting luminescence nanoprobe operating around 1,800 nm for NIR-IIb and c bioimaging. Nat. Commun. 14, 1079 (2023).
- Arús, B. A. et al. Shortwave infrared fluorescence imaging of peripheral organs in awake and freely moving mice. Front. Neurosci 17, 1135494 (2023).
- Kim, T., O'Brien, C., Choi, H. S. & Jeong, M. Y. Fluorescence molecular imaging systems for intraoperative image-guided surgery. Appl. Spectrosc. Rev. 53, 349–359 (2018).
- Wan, H. et al. A bright organic NIR-II nanofluorophore for three-dimensional imaging into biological tissues. *Nat. Commun.* 9, 1171 (2018).
- Yu, W. et al. NIR-II fluorescence in vivo confocal microscopy with aggregation-induced emission dots. Sci. Bull. 64, 410–416 (2019).
- Yu, J. et al. Intravital confocal fluorescence lifetime imaging microscopy in the second near-infrared window. Opt. Lett. 45, 3305–3308 (2020).
- Xia, F. et al. Short-wave infrared confocal fluorescence imaging of deep mouse brain with a superconducting nanowire single-photon detector. ACS Photon. 8, 2800–2810 (2021).
- 77. Kobat, D., Horton, N. & Xu, C. In vivo two-photon microscopy to 1.6-mm depth in mouse cortex. J. Biomed. Opt. 16, 106014 (2011).
- Horton, N. G. et al. In vivo three-photon microscopy of subcortical structures within an intact mouse brain. *Nat. Photon.* 7, 205–209 (2013).
- Gu, M., Gan, X., Kisteman, A. & Xu, M. G. Comparison of penetration depth between two-photon excitation and single-photon excitation in imaging through turbid tissue media. *Appl. Phys. Lett.* 77, 1551–1553 (2000).
- Huisken, J., Swoger, J., Del Bene, F., Wittbrodt, J. & Stelzer, E. H. K.
 Optical sectioning deep inside live embryos by selective plane illumination microscopy. Science 305, 1007–1009 (2004).
- Liu, T.-L. et al. Observing the cell in its native state: imaging subcellular dynamics in multicellular organisms. Science 360, eaaq1392 (2018).
- 82. Yu, H. et al. Combining near-infrared excitation with Swept Confocally-Aligned Planar Excitation (SCAPE) microscopy for fast, volumetric imaging in mouse brain. In *Biophotonics Congress:*Biomedical Optics Congress 2018 (Microscopy/Translational/Brain /OTS). BF3C.3 (Optica Publishing Group, 2018).
- Olarte, O. E. et al. Image formation by linear and nonlinear digital scanned light-sheet fluorescence microscopy with Gaussian and Bessel beam profiles. *Biomed. Opt. Express* 3, 1492–1505 (2012).
- 84. Nylk, J. et al. Light-sheet microscopy with attenuation-compensated propagation-invariant beams. *Sci. Adv.* **4**, eaar4817 (2018).
- Herisson, F. et al. Direct vascular channels connect skull bone marrow and the brain surface enabling myeloid cell migration. Nat. Neurosci. 21, 1209–1217 (2018).
- Wang, F. et al. Scanning superlens microscopy for non-invasive large field-of-view visible light nanoscale imaging. *Nat. Commun.* 7, 13748 (2016).
- 87. Liu, P. et al. Airy beam assisted NIR-II light-sheet microscopy. *Nano Today* **47**, 101628 (2022).
- Gustafsson, M. G. L. Nonlinear structured-illumination microscopy: wide-field fluorescence imaging with theoretically unlimited resolution. *Proc. Natl Acad. Sci. USA* 102, 13081–13086 (2005).

- 89. Hong, G. et al. Near-Infrared II fluorescence for imaging hindlimb vessel regeneration with dynamic tissue perfusion measurement. *Circ. Cardiovasc. Imag.* **7**, 517–525 (2014).
- 90. Qi, J. et al. Real-time and high-resolution bioimaging with bright aggregation-induced emission dots in short-wave infrared region. *Adv. Mater.* **30**, 1706856 (2018).
- 91. Liu, H. et al. Atomic-precision gold clusters for NIR-II imaging. *Adv. Mater.* **31**, 1901015 (2019).
- Zhang, X.-D. et al. Traumatic brain injury imaging in the second near-infrared window with a molecular fluorophore. *Adv. Mater.* 28, 6872–6879 (2016).
- 93. Chatterjee, A., Serniak, N. & Czerniecki, B. J. Sentinel lymph node biopsy in breast cancer: a work in progress. *Cancer J.* **21**, 7–10 (2015).
- 94. Tian, R. et al. Multiplexed NIR-II probes for lymph node-invaded cancer detection and imaging-guided surgery. *Adv. Mater.* **32**, 1907365 (2020).
- 95. Li, M. et al. Near-infrared-II ratiometric fluorescence probes for non-invasive detection and precise navigation surgery of metastatic sentinel lymph nodes. *Theranostics* **12**, 7191–7202 (2022).
- 96. Hu, Z. et al. First-in-human liver-tumour surgery guided by multispectral fluorescence imaging in the visible and near-infrared-I/II windows. *Nat. Biomed. Eng.* **4**, 259–271 (2020).
- 97. Morlandt, A. B. et al. Fluorescently labeled Cetuximab-IRDye800 for guided surgical excision of ameloblastoma: a proof of principle study. *J. Oral. Maxil. Surg.* **78**, 1736–1747 (2020).
- 98. Suo, Y. et al. NIR-II fluorescence endoscopy for targeted imaging of colorectal cancer. *Adv. Healthc. Mater.* **8**, 1900974 (2019).
- Girard, J.-P., Moussion, C. & Förster, R. HEVs, lymphatics and homeostatic immune cell trafficking in lymph nodes. *Nat. Rev. Immunol.* 12, 762–773 (2012).
- 100. He, L. et al. Engineering of reversible NIR-II redox-responsive fluorescent probes for imaging of inflammation in vivo. *Angew. Chem. Int. Ed.* **61**, e202211409 (2022).
- Lan, Q. et al. Polymethine molecular platform for ratiometric fluorescent probes in the second near-infrared window. J. Am. Chem. Soc. 144, 21010–21015 (2022).
- 102. Miao, J. et al. An activatable NIR-II fluorescent reporter for in vivo imaging of amyloid-β plaques. Angew. Chem. Int. Ed. 62, e202216351 (2023).
- 103. He, Y. et al. NIR-II cell endocytosis-activated fluorescent probes for in vivo high-contrast bioimaging diagnostics. *Chem. Sci.* 12, 10474–10482 (2021).
- 104. Chen, Z. et al. Design and synthesis of a small molecular NIR-II chemiluminescence probe for in vivo-activated H_2S imaging. *Proc. Natl Acad. Sci. USA* **120**, e2205186120 (2023).
- 105. Fang, Z. et al. Oxyhaemoglobin saturation NIR-IIb imaging for assessing cancer metabolism and predicting the response to immunotherapy. *Nat. Nanotechnol* 19, 124–130 (2024).
- 106. Tian, R. et al. Rational design of a super-contrast NIR-II fluorophore affords high-performance NIR-II molecular imaging guided microsurgery. *Chem. Sci.* **10**, 326–332 (2019).
- Wang, P. et al. NIR-II nanoprobes in-vivo assembly to improve image-guided surgery for metastatic ovarian cancer. *Nat. Commun.* 9, 2898 (2018).
- 108. Fan, X. et al. Aggregation-induced emission (AIE) nanoparticles-assisted NIR-II fluorescence imaging-guided diagnosis and surgery for inflammatory bowel disease (IBD). Adv. Healthc. Mater. 10, 2101043 (2021).
- 109. Antaris, A. L. et al. A high quantum yield molecule-protein complex fluorophore for near-infrared II imaging. *Nat. Commun.* **8**, 15269 (2017).
- 110. Wu, Y. et al. First clinical applications for the NIR-II imaging with ICG in microsurgery. *Front. Bioeng. Biotechnol.* **10**, 1042546 (2022).

- Carr, J. A., Valdez, T. A., Bruns, O. T. & Bawendi, M. G. Using the shortwave infrared to image middle ear pathologies. *Proc. Natl Acad. Sci. USA* 113, 9989–9994 (2016).
- 112. Shi, X. et al. Zn-doping enhances the photoluminescence and stability of PbS quantum dots for in vivo high-resolution imaging in the NIR-II window. *Nano Res.* **13**, 2239–2245 (2020).
- 113. Magdaong, N. C. M., Niedzwiedzki, D. M., Goodson, C. & Blankenship, R. E. Carotenoid-to-bacteriochlorophyll energy transfer in the LH1–RC core complex of a bacteriochlorophyll b containing purple photosynthetic bacterium blastochloris viridis. J. Phys. Chem. B 120, 5159–5171 (2016).
- Chang, Z. et al. Near infrared-II fluorescent protein for in-vivo imaging. Preprint at https://www.biorxiv.org/content/10.1101/ 2022.03.04.482971v1.full (2022).
- Ma, Z., Wang, F., Wang, W., Zhong, Y. & Dai, H. Deep learning for in vivo near-infrared imaging. Proc. Natl Acad. Sci. USA 118, e2021446118 (2021).
- Tummers, W. S. et al. Regulatory aspects of optical methods and exogenous targets for cancer detection. *Cancer Res.* 77, 2197–2206 (2017).
- 117. Scheuer, W., van Dam, G. M., Dobosz, M., Schwaiger, M. & Ntziachristos, V. Drug-based optical agents: infiltrating clinics at lower risk. *Sci. Transl. Med.* **4**, 134ps111 2012).
- DSouza, A., Lin, H., Henderson, E., Samkoe, K. & Pogue, B. Review of fluorescence guided surgery systems: identification of key performance capabilities beyond indocyanine green imaging. *J. Biomed. Opt.* 21, 080901 (2016).
- 119. Wang, M. et al. Comparing the effective attenuation lengths for long wavelength in vivo imaging of the mouse brain. *Biomed. Opt. Express* **9**, 3534–3543 (2018).

Acknowledgements

H. Dai acknowledges the National Institutes of Health (NIH DP1-NS-105737) as the sole funding source for the Dai group's work reviewed in this paper.

Competing interests

The authors declare no competing interests.

Additional information

Correspondence and requests for materials should be addressed to Hongiie Dai.

Peer review information *Nature Photonics* thanks Jun Qian and the other, anonymous, reviewer(s) for their contribution to the peer review of this work.

Reprints and permissions information is available at www.nature.com/reprints.

Publisher's note Springer Nature remains neutral with regard to jurisdictional claims in published maps and institutional affiliations.

Springer Nature or its licensor (e.g. a society or other partner) holds exclusive rights to this article under a publishing agreement with the author(s) or other rightsholder(s); author self-archiving of the accepted manuscript version of this article is solely governed by the terms of such publishing agreement and applicable law.

© Springer Nature Limited 2024